Check for updates

Tailoring resistive switching in ultra-thin tellurium films by interface engineering

Sara Ghomi,†[a] Carlo Grazianetti, †[a] Andrea Serafini,[b] Paolo Targa,[b] Davide Codegoni,[b] Alessio Lamperti,[a] Christian Martella *[a] and Alessandro Molle *[a]

The use of two-dimensional or nanoscaled materials as active medium in resistive switching (RS) is becoming more and more frequent in the neuromorphic and in-memory computing. Although many works have focused their attention on the RS mechanism of the materials, less attention is devoted to understanding the role of the interfaces with the metallic electrodes, especially when the electrode is also used as substrate for the growth of the material. Indeed, a low temperature growth of the active material on the largest possible metallic substrate would greatly improve the scalability and compatibility with back-end-of-line processing of the resulting memristive devices. Here, we report that tellurium grown by vapour transport deposition at 100 °C on gold substrate improves its RS when the surface of the Au(111) shows the well-known herringbone reconstruction. Indeed, the morphology of the nanoscaled tellurium is influenced by the gold surface reconstruction and, in turn, its RS probed by conductive atomic force

New concepts

This research introduces a novel perspective on interface engineering at the nanoscale to optimize resistive switching in tellurium-based devices. Unlike conventional approaches that focus solely on material composition, our concept emphasizes how the atomic-scale structure and reconstruction of the gold substrate, particularly the herringbone surface pattern, can dramatically influence the morphology and electrical behavior of deposited tellurium films. By exploiting the reconstructed gold surface, we demonstrate a new pathway for controlling the interface at the atomic level, which in turn happens to boost the resistive switching performances of the deposited tellurium. The core innovation of our approach, compared to existing studies, lies in recognizing that interface atomic arrangement, and not just the bulk material, can serve as a critical knob for enhancing device performance. This paradigm shift, from viewing interfaces as passive boundaries to active atomic landscapes, opens fresh avenues for designing energy-efficient resistive memory and neuromorphic systems. It paves the way for integrating surface reconstruction phenomena into the broader field of nanoelectronics, offering fundamentally new insights into how the atomic organization of matter at the nanoscale governs macroscopic device functionalities.

microscopy. By comparison with the un-reconstructed surface, a non-negligible reduction of the set and reset voltages is observed. These results demonstrate that proper interface engineering between the material and electrodes might turn out to be as important as the material itself for the memristive performance.

Introduction

The quest for energy-efficient, reliable, and scalable resistive switching (RS) devices has triggered intense research into the development of novel functional materials, architectures and interfaces.[1–4] Among these, chalcogenides like tellurium have shown great promise for next-generation non-volatile memory,

Christian Martella

Our first experience with Nanoscale Horizons dates back to 2022, when we published original results on the thermal and optical properties of silicene nanosheets. Again in 2023, beyond the quest for innovative stabilization routes of silicene enabling its technology transfer, we found in Nanoscale Horizons a venue where conceptual novelty is truly valued. Its editorial vision makes it a privileged platform for disruptive ideas. With this spirit, we now celebrate the 10th anniversary by contributing an article unveiling an unprecedented effect of substrate proximity on the resistive switching behavior of nanoscale tellurium.

[a] CNR IMM, Unit of Agrate Brianza, via C. Olivetti 2, Agrate Brianza 20864, Italy. E-mail: christian.martella@cnr.it, alessandro.molle@cnr.it

[b] STMicroelectronics, via C. Olivetti 2, Agrate Brianza 20864, Italy

† Equal contribution.

artificial synapses, and neuromorphic applications.[5–8] The quality of the interface between the active switching material and its conductive substrate is a crucial component that affects how well these devices work.[9,10]

Gold is commonly used as a substrate in electronic devices because of its remarkable electrical conductivity and natural resistance to oxidation.[11,12] Furthermore, the single-crystalline Au(111) surface provides a distinct and repeatable platform for epitaxial growth of large-area wetting films or ease of layer transferability when supported on delaminable substrates like mica. Furthermore, gold possesses the peculiar characteristic of a surface reconstruction like the semiconductors. Indeed, gold is the only metal where the close-packed (111) surface reconstructs into so-called herringbone $(22 \times \sqrt{3})$ pattern.[13,14] Such a surface reconstruction makes the gold surface appealing for multiple applications, in particular it turns out to be an energetically favorable template for organic molecular self-assembly[15] or low-dimensional materials growth.[16] However, despite the potential implications for film crystallinity and device performance, the effect played by the gold surface when used as electrode in devices is scarcely investigated thus far. Nonetheless, gold has been demonstrated to be a viable substrate for the growth of thin tellurium films at temperature compatible with back-end-of-line (BEOL) standard industrial processes.[17] The direct growth on the gold substrate marks also a significant breakthrough for the manufacturing of tellurium-based diodes with memristive behavior. Since the underlying gold concomitantly serves as both the supporting substrate and the bottom electrode, no additional transfer process step is therefore required in the streamline of the fabrication.[18] The process scheme for assessing gold-supported tellurium films in view of memristive applications builds upon the condensation-driven direct growth of tellurium and their subsequent investigation by conductive atomic force microscopy (c-AFM). In this configuration, the conductive tip of the AFM directly acts as the top electrode, enabling point conduction spectroscopy to probe the local RS characteristics of the films without the need for a device architecture (Fig. S1 of SI). This approach provides a purely materials-level perspective, offering fundamental insights into the switching behavior of tellurium. While the encapsulation of such films into a diode-like structure could be envisioned as a possible route toward prototypical memristor devices, the focus of the present study remains on the fundamental characterization achieved through c-AFM.

We recently showed that tellurium growth evolution on gold is dramatically affected by the parametric conditions of tellurium vapour exposure in low vacuum with the substrate temperature discriminating a low-temperature absorption regime of elemental tellurium growth (below 350 °C) from a chemisorption regime of gold tellurization (above 350 °C).[17] If the substrate temperature is the driving factor for such a phenomenology, the structural details of the host gold surface can dictate the morphology of the tellurium overlayers, and the resulting interface is ultimately expected to influence the vertical electrical transport through the tellurium-based diode owing to proximity effects, namely interaction of surface gold atoms with the tellurium body under applied electrical bias. Indeed, single atoms at the gold surface are known to undergo substitutional atomic exchange with a 2D MoS_2 layer therein triggering local non-volatile switching that is eventually responsible for the memristive behavior in the final atomristor device.[19,20] Therefore, local protrusions and non-uniformities at the gold surface level are expected to boost or limit possible interactions with the overgrown tellurium layer ending up in the activation/inhibition of conductive path through the tellurium body. To discriminate proximity effects of this kind more closely, two paradigmatic cases of ordered and disordered interfaces between a gold substrate and a deposited tellurium film are investigated by comparing non-reconstructed Au(111)/Mica with a herringbone-reconstructed single-crystalline Au(111)/Mica substrate hosting a tellurium layer grown with the same process scheme.

The morphological, structural, and electrical features of the resultant films are comprehensively characterized using AFM, X-ray diffraction (XRD), transmission electron microscopy (TEM), Raman spectroscopy, and c-AFM. Our findings show that substrate preparation not only changes the surface morphology (transforming small grain structures into micrometre-scaled terraces), but it also increases Te crystallinity and results in more energy-efficient and uniform RS behavior. These findings highlight the significance of interface engineering in enhancing the performance of tellurium-based RS devices and provide useful insights for the design of future nanoelectronics systems.

Results and discussion

Aiming at studying the role of the interface in a memristive device where tellurium is grown on top of gold, two different gold surfaces were considered. Specifically, thin (300 nm) single crystalline Au(111) on cleavable Mica substrates were used. In one case, the substrate was used as is, without any surface treatment. In another case, the growth of tellurium was also investigated on the surface that underwent Ar^+ sputtering and annealing at 500 °C to show a herringbone-reconstructed crystalline Au(111) surface (hereafter termed hr-Au(111)/Mica).

The deposition of tellurium on these two substrates was performed at the same growth conditions by vapour transport deposition (see Experimental section). Based on process calibrations optimized for thickness control, the deposition on both substrates was carried out to obtain a tellurium layer with a thickness in the range of 7 to 10 nm, as confirmed by the AFM and scanning TEM (STEM) analyses shown in Fig. S2 and S3 in SI. Moreover, to investigate the spatial distribution and uniformity of tellurium deposition on the gold substrate, energy-dispersive X-ray spectroscopy (EDX) mapping was performed using TEM. The chemical analysis performed by EDX revealed that the tellurium deposition is more homogeneously distributed on the hr-Au(111)/Mica surface than on the bare Au(111)/Mica. The intensity profile of the signals, corresponding to the Te and Au elements, suggests that in both the cases Te forms a distinct overlayer on the surface (Fig. S3 in SI). To get a closer insight into the morphological features of the grown material,
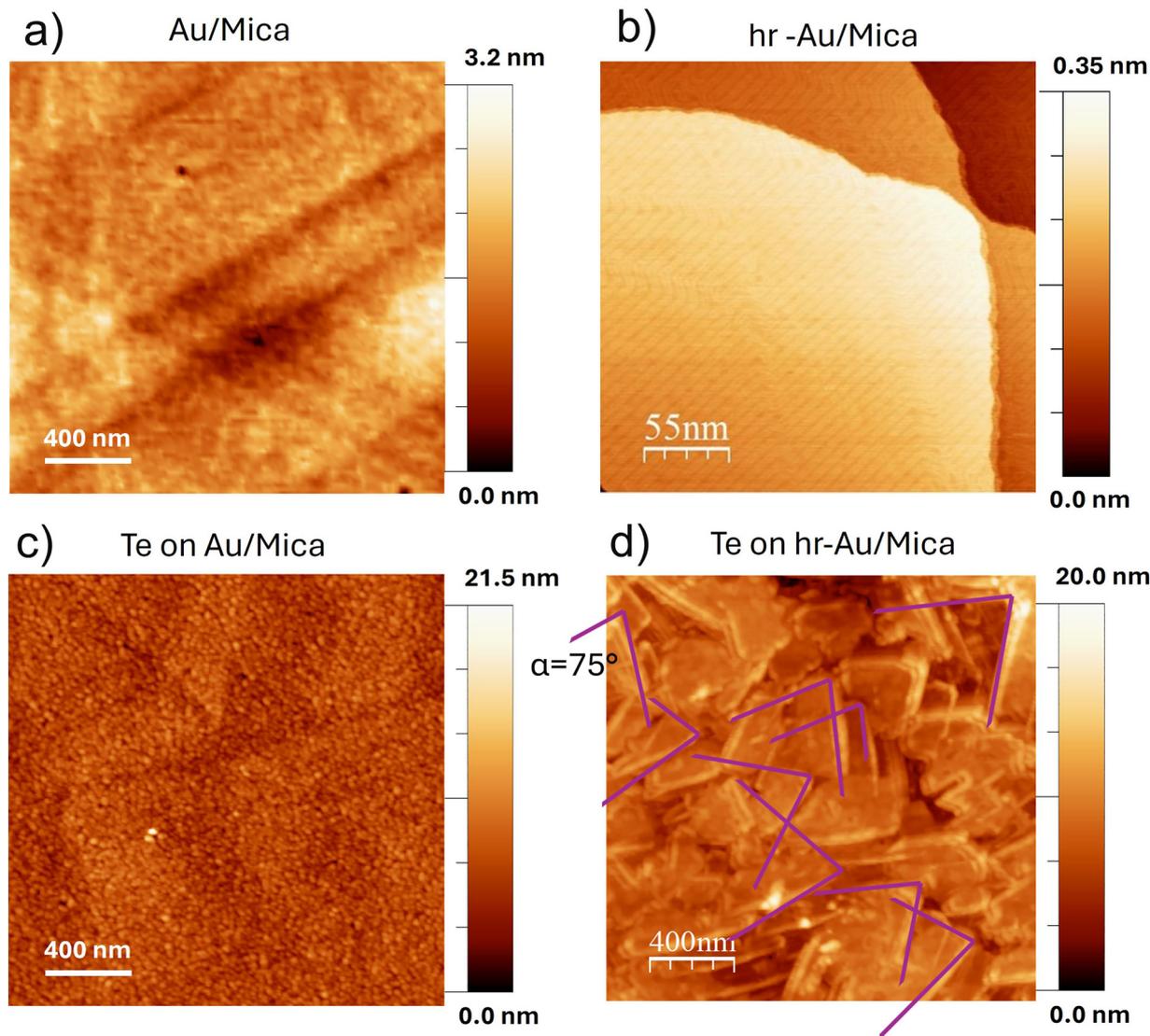
Fig. 1 AFM topography image of (a) Au(111)/Mica substrate and (c) Te deposited on Au(111)/Mica substrate (b) Au(111)/Mica substrate and (d) Te deposited on reconstructed Au(111)/Mica substrate. The purple graphical marks are guides for the eye to identify preferential 75° angular shaped Te edges grown on the hr-Au(111)/Mica substrate.

topographic AFM characterization was carried out on the substrates before and after the growth of the deposited tellurium as summarized in Fig. 1. In the former case, *i.e.* without surface reconstruction, the crystalline Au(111)/Mica substrate exhibits a morphology with a very smooth surface and root mean square (RMS) roughness of 0.4 nm. After the deposition, tellurium on Au(111)/Mica shows the formation of small grains with an average grain size of 22 ± 5 nm and RMS roughness of 1.5 nm. In the second case, the surface of Au(111)/Mica substrate was prepared in ultra-high vacuum (UHV) in order to induce the reconstructed herringbone pattern as shown in the scanning tunneling microscopy (STM) topography of Fig. 1b. The deposition on this type of substrate yielded a distinct morphology consisting of tellurium structures on the herringbone pattern. The topography of Fig. 1d shows a dense distribution of micrometre-scaled crystallite structures on the surface organized

in a terraces fashion. Considering the terraces morphologies the RMS roughness of the 2 μm × 2 μm image of Fig. 1d increases up to 2.1 nm compared to the previous case of non-reconstructed gold surface. Moreover, the shapes of the crystallites present straight edges with random orientations. However, by a closer inspection of different maps, the tellurium structures show preferential angular shaped morphologies with typical angle of ~75°, as clearly identified in the AFM topographies of Fig. 1d and Fig. S4 in SI. These findings closely match those reported in STM investigations that elucidate the epitaxial growth behavior of magnetic elements such as Ni, Co, and Fe on hr-Au(111) surfaces.[21-23] In these studies, STM imaging across varying surface coverages consistently revealed that, at room temperature, nucleation initiates preferentially at the domain boundaries of the zigzag reconstruction, specifically at the kink sites within the herringbone elbows.

In order to assess the vibrational properties of the tellurium structures obtained in both cases, with a particular attention to their uniformity on the cm^2 deposition area, Raman spectroscopy was conducted on the deposited tellurium films, Fig. 2. Fig. 2a compares the Raman spectra of tellurium samples deposited on Au(111)/Mica and hr-Au(111)/Mica, green and magenta curves respectively. The spectra represent the two distinct Raman modes of tellurium: out-of-plane vibrational mode A^1 at 122 cm^{-1} and in-plane vibrational mode E^2 at 141 cm^{-1}.[24] Interestingly, no marked differences in the vibrational properties can be observed despite the different morphology of the tellurium structures. The consistent position of the Raman modes in both cases indicates that the thickness of the deposited tellurium remains within the same range, regardless of the surface reconstruction of the gold substrate or the resulting morphological differences observed in the AFM topographies.[25] For a more thorough comparison, the full-width-half-maximum (FWHM) of A^1 and E^2 peaks are plotted in Fig. 2b, showing the average and standard deviations of these modes for the two different surfaces. It can be observed that the FWHM of A^1 and E^2 peaks and their variations for tellurium deposited on hr-Au(111)/Mica is the lowest suggesting an improved crystallinity compared to the Te deposited on Au(111)/Mica without any prior preparation.

To further study the uniformity of the deposited tellurium on the two surfaces at the 1 cm^2 scale, the positional Raman spectra were collected at nine equidistant points on each sample at a 0.3 cm distance. Fig. S5 of the SI shows the spatial distribution of A^1 Raman peak intensity, normalized to the maximum A^1 peak intensity. The results show uniform deposition over the substrate for all the samples with less than 2%

variation of the A^1 peak intensity shading across different samples.

While the analysis of the Raman mode FWHM provides only a preliminary indication of improved crystallinity in tellurium grown on reconstructed gold surfaces, the XRD investigation at fixed grazing incidence angle reported in Fig. 2c allows for a more detailed and comprehensive assessment of the structural differences between the two samples. We note that, compared with the sample grown on the unreconstructed Au surface, the tellurium grown on the reconstructed Au surface exhibit sharper and more intense peaks, indicating enhanced crystalline order. In both the patterns, the peak at 38° corresponding to the Te (102) orientation is the most intense, other main diffraction peaks appear at 2θ values of ∼45°, 46.5°, 51.5° corresponding to the (003), (200) and (103) planes of tellurium respectively.[26,27]

Point conductivity spectroscopy empowered by c-AFM is an effective route to locally measure the electrical switching behavior of Te films on the two different surfaces. For the Te on unreconstructed Au(111)/Mica sample, an average set voltage of 1.4 V (±0.2 V) and reset voltage of −1.9 V (±0.6 V) are measured over hundred curves, Fig. 3a. In contrast, the Te on hr-Au(111)/Mica exhibits a lower average set (1 ± 0.1 V) and reset (−1.2 ± 0.3 V) voltages, Fig. 3b. Hence, when no preparation is performed on the substrate, higher voltages are needed to induce the observed RS behaviour (Fig. 3c). Conversely, more energy-efficient switching with a narrower spread of values occurs when the herringbone reconstruction is induced. As a matter of fact, this improved behaviour is due to the substrate preparation, which in turn enhance interface quality, reduce defect and trap densities, and likely promote more uniform conductive path for ion migration or filament formation/rupture. Overall, these results imply that optimizing the interfacial properties through substrate preparation can lead to more reliable and lower-energy RS in tellurium-based devices.

To get a deeper insight into the differences between the two devices, a detailed analysis on the RS curves is reported in Fig. 4. For the Te on Au(111)/Mica sample during the set process, the high resistance state (HRS) initially exhibits a linear relationship (slope ≈1.4), consistent with ohmic conduction where the current scales directly with voltage ($I \propto V$). As the voltage increases, the slope transitions to a quadratic behavior (slope ≈2.2), which is characteristic of space-charge-limited conduction (SCLC) in the trap-unfilled regime. At even higher voltages, the slope abruptly increases to about 5.8, indicating a transition to the trap-filled limit of SCLC. On the other hand, the low resistance state (LRS) shows a slope of approximately ≈2.1 in the high-voltage regime that decreases to around ≈1.2 at low voltages. This behavior, particularly the near-linear (ohmic) conduction at lower voltages, is compatible with a filamentary switching mechanism as reported in previous studies.[28–32] A similar sequence of conduction mechanisms is observed during the reset process. In the case of Te films on hr-Au(111)/Mica substrates, the double-logarithmic I–V analysis reveals notable differences. In the LRS, a slope of ≈1.2 in the full voltage range indicates ohmic behavior, suggesting that
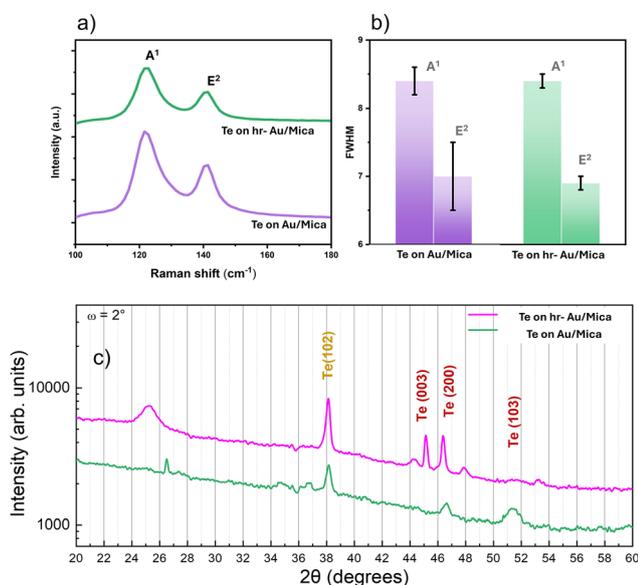

Fig. 2 (a) Raman spectra acquired on Te deposited on Au(111)/Mica and hr-Au(111)/Mica (b) comparison of the mean value and standard deviations of the A^1 and E^2 peak FWHM. (c) Grazing incident XRD pattern of the tellurium deposition on Au(111)/Mica (green curve) and on hr-Au(111)/Mica (magenta curve).
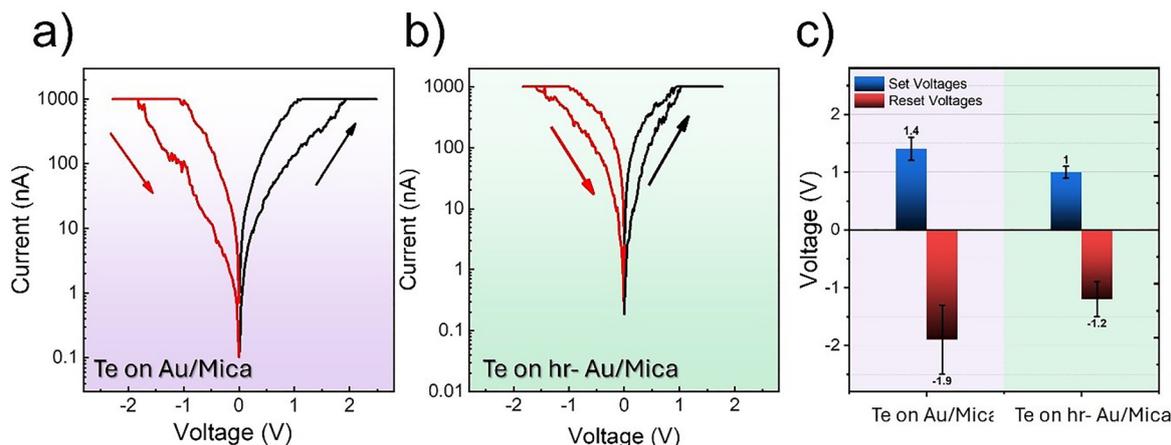
Fig. 3 (a) and (b) $I{-}V$ characteristics obtained by c-AFM performed on Te/Au(111)/Mica and Te/hr-Au(111)/Mica samples. (c) Comparison of the average values and standard deviations of set and reset voltages.

conductive filament formation governs the conduction. However, the HRS shows a more gradual evolution: the initial slope is about 1.3, which then increases to 2.5, and finally reaches 4.8 at higher voltages. This progressive change in the slope suggests
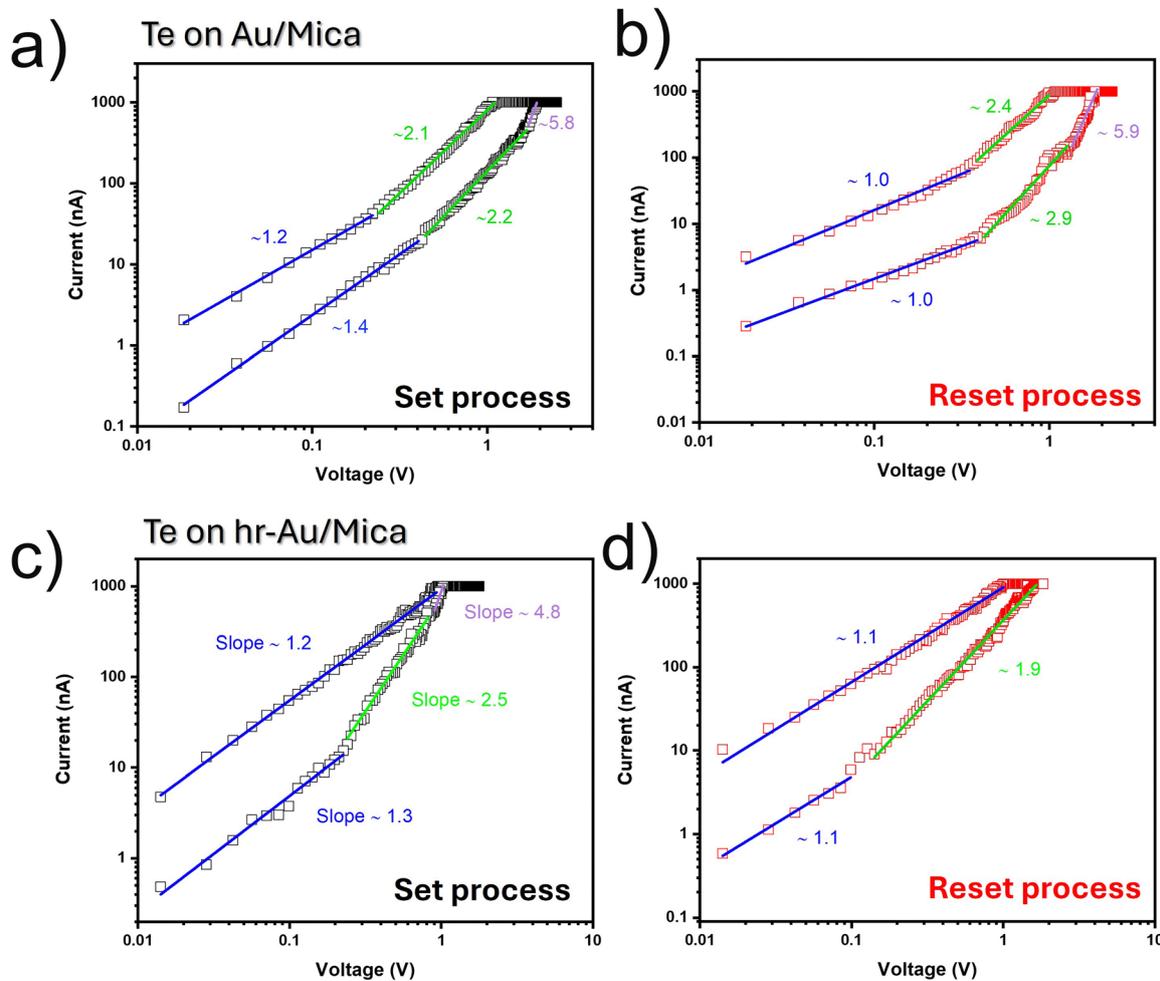

Fig. 4 Double-logarithmic plots of the $I{-}V$ characteristics of ultra-thin tellurium films grown on Au (111)/Mica in (a) positive bias region (set process) and (b) negative bias region (reset process). Double-logarithmic plots of the $I{-}V$ characteristics of ultra-thin tellurium films grown on hr-Au (111)/Mica in (c) positive bias region (set process) and (d) negative bias region (reset process).

that, in the reconstructed surface, the transition from ohmic to SCLC conduction is more gradual than in the unreconstructed Au/Mica case. We interpret such differences as due to modifications in the interface between gold electrode and nanoscaled tellurium that can affect the filament formation and therefore the RS. The preparation of Au (111)/Mica surface by inducing a herringbone reconstruction with cycles of Ar$^+$ sputtering and annealing improves the electrical switching behavior of subsequently deposited Te films. This is evidenced by the observation of a lower absolute set and reset switching voltage pointing to more energy-efficient switching in Te films grown on hr-Au(111)/Mica film. The herringbone reconstruction of the Au(111) surface promotes crystalline order and RS energetically favorable conditions for the Te deposition. The well-known herringbone reconstruction can facilitate the epitaxial growth of Te leading to film with larger crystalline domains, reduced grain boundaries, and consequently enhanced electrical switching characteristics in Te films deposited on hr-Au(111)/Mica substrate.

Conclusions

In summary, we reported the influence of the surface termination of the bottom electrode in RS devices. Our comparative analysis between unreconstructed and reconstructed Au(111) surfaces highlights that the optimization of the Te/Au interface can significantly improve the structural and electrical properties of tellurium-based devices by selecting an ordered registry, namely the herringbone reconstruction, as an interface configuration that is prone to improve the inherent RS characteristic of nanoscale tellurium in terms of reduced set and reset voltage. These findings point out that in the fabrication of memristive devices attention should be paid to the role of the interfaces in addition to the ongoing effort to find more efficient materials to act as RS. Indeed, the proper functioning of a RS material could be undermined by a poor interfacing with the metal electrodes and then considered a bad candidate for memristive applications. Intriguingly, the use of thin Au films on Mica substrates makes it possible to introduce these devices in flexible applications, like wearable or healthcare electronics. Therefore, a concomitant study of materials and interfaces is crucial for the development of energy-efficient RS memory devices.

Experimental

Materials growth

Vapor transport deposition was used on two different gold surfaces of commercial Au(111) single crystal with nominal thickness ~ 300 nm on Mica substrate. The unreconstructed Au(111)/Mica samples were used as provided by the supplier, while the reconstructed Au(111)/Mica substrate was loaded into a UHV system (base pressure 10^{-10} mbar) where three cycles of sputtering and annealing were carried out until the herringbone pattern appeared in the STM topography (Fig. 1). Sputtering with Ar$^+$ ions was performed at 1.5 kV and 10 mA for 15 minutes. The sample was annealed at 500 °C for 30 minutes until the base

pressure was restored. STM was performed at room temperature with an electrochemically etched polycrystalline W tip at setpoint $V = 0.6$ V and $I = 1.9$ nA. The deposition reactor consists of a double furnace system equipped with a quartz tube reactor of 2″ diameter. Tellurium (Te) powder (40 mg: 99.997%, Sigma Aldrich, Darmstadt, Germany) was used as a precursor. The tellurium powder was placed in a ceramic boat in the center of the upstream furnace, and the gold substrate was cut in 3×1 cm^2 dimensions, kept on a ceramic boat (face up), and positioned 18 cm away from the Te precursor reference. The temperatures of 440 °C set for the upstream and 100 °C set for the downstream, with a 100 sccm Ar/H$_2$ flux (H$_2$ 4% volume) as a carrier gas that was flowing for 30 minutes growth time.

Atomic force microscopy (AFM). The morphology of the samples was investigated in tapping mode using commercial AFM (Bruker Dimension Edge). Topographies were acquired in tapping mode using ultra-sharp silicon tips (TESPA-V2 Bruker radius of curvature 7 nm nominal frequency 320 kHz) Statistical parameters of the surface morphology, such RMS roughness, were derived by means of freely available software (WSxM, Gwyddion).[33]

Conductive AFM (C-AFM). The commercial AFM (Bruker Dimension Edge) equipped with a TUNA electrometer with 1 pA to 1 μA current range was used to characterize the electrical properties of the samples at the local scale. A conductive diamond-coated tip (CDT-CONTR, nanosensors, with a radius of curvature between 100 and 200 nm) was used to scan over the surface of the sample in ambient condition.

Raman spectroscopy. The vibrational properties of the deposited sample were verified in z-backscattering geometry using a Renishaw spectrometer (In-Via) equipped with a solid-state laser source of excitation wavelength 514 nm/2.41 eV. The laser source is coupled with an optical microscope and objective with numerical aperture = 0.75 and magnification 50×. The laser power on the sample was kept below 5 mW to avoid sample damage.

X-ray diffraction (XRD). Diffraction at grazing incidence angle $\omega = 2°$ have been performed using an XRD3000 diffractometer (Italstructure) with monochromated X-ray Cu Kα radiation (wavelength 0.154 nm) and beam size defined by slits aperture of 0.1×4 mm^2.

Transmission electron microscopy (TEM), EDX. The samples were extensively investigated utilizing STEM related techniques such as dark-field STEM (DF-STEM) for the microstructural characterization, while the chemical properties were investigated by STEM EDX. DF-STEM and EDX analyses were carried out on electron-transparent lamella obtained using focused ion beam thinning of cross-section TEM lamellae. The lamellae preparation was performed using a Thermofisher Helios G5UX FIB. In all cases, particular care was taken to limit the heating and ballistic effects of ion irradiation on the samples during the final ion milling steps. In particular, a new advanced approach has been applied, reducing currents and energies progressively from a value of 30 keV to a value of low keV in order to avoid material amorphization and damage. The STEM images were performed with a Thermofisher Themis Z G3

aberration-corrected scanning transmission electron microscope equipped with an electron gun monochromator operating at 200 kV acceleration voltage. To limit the electron beam damage, all the STEM images were acquired with a low beam current (0.5 nA).

Author contributions

Sara Ghomi: formal analysis; investigation; software; validation; visualization; writing – original draft; writing – review & editing. Carlo Grazianetti: conceptualization; formal analysis; funding acquisition; investigation; methodology; validation; visualization; writing – original draft; writing – review & editing. Andrea Serafini: investigation; writing – review & editing. Paolo Targa: investigation; writing – review & editing. Davide Codegoni: investigation; writing – review & editing. Alessio Lamperti: formal analysis; investigation; supervision; writing – review & editing. Christian Martella: conceptualization; data curation; formal analysis; funding acquisition; investigation; methodology; supervision; validation; visualization; writing – original draft; writing – review & editing. Alessandro Molle: conceptualization; data curation; formal analysis; funding acquisition; investigation; methodology; project administration; resources; supervision; validation; visualization; writing – original draft; writing – review & editing.

Conflicts of interest

There are no conflicts to declare.

Data availability

The data supporting this article have been included as part of the supplementary information (SI). Data include additional AFM, EDX and TEM investigations along with spatial Raman mapping of the samples. Supplementary information is available. See DOI: **https://doi.org/10.1039/d5nh00427f**.

Acknowledgements

Notes and references

1 D. V. Christensen, R. Dittmann, B. Linares-Barranco, A. Sebastian, M. L. Gallo, A. Redaelli, S. Slesazeck, T. Mikolajick, S. Spiga, S. Menzel, I. Valov, G. Milano, C. Ricciardi, S.-J. Liang, F. Miao, M. Lanza, T. J. Quill, S. T. Keene, A. Salleo, J. Grollier, D. Marković, A. Mizrahi, P. Yao, J. J. Yang, G. Indiveri, J. P. Strachan, S. Datta, E. Vianello, A. Valentian, J. Feldmann, X. Li, W. H. P. Pernice, H. Bhaskaran, S. Furber, E. Neftci, F. Scherr, W. Maass, S. Ramaswamy, J. Tapson, P. Panda, Y. Kim, G. Tanaka, S. Thorpe, C. Bartolozzi, T. A. Cleland, C. Posch, S. Liu, G. Panuccio, M. Mahmud, A. N. Mazumder, M. Hosseini, T. Mohsenin, E. Donati, S. Tolu, R. Galeazzi, M. E. Christensen, S. Holm, D. Ielmini and N. Pryds, *Neuromorph. Comput. Eng.*, 2022, **2**, 022501.

2 D. Ielmini and H.-S. P. Wong, *Nat. Electron.*, 2018, **1**, 333–343.

3 C. Liu, H. Chen, S. Wang, Q. Liu, Y.-G. Jiang, D. W. Zhang, M. Liu and P. Zhou, *Nat. Nanotechnol.*, 2020, **15**, 545–557.

4 F. Ferrarese Lupi, G. Milano, A. Angelini, M. Rosero-Realpe, B. Torre, E. Kozma, C. Martella and C. Grazianetti, *Adv. Funct. Mater.*, 2024, **34**, 2403158.

5 L. Li, G. Zhang, M. Younis, T. Luo, L. Yang, W. Jin, H. Wu, B. Xiao, W. Zhang and H. Chang, *ACS Appl. Electron. Mater.*, 2024, **6**, 2161–2167.

6 S. Ghomi, C. Martella, Y. Lee, P. H.-P. Chang, P. Targa, A. Serafini, D. Codegoni, C. Massetti, S. Gharedaghi, A. Lamperti, C. Grazianetti, D. Akinwande and A. Molle, *Adv. Sci.*, 2025, **12**, 2406703.

7 Y. Yang, M. Xu, S. Jia, B. Wang, L. Xu, X. Wang, H. Liu, Y. Liu, Y. Guo, L. Wang, S. Duan, K. Liu, M. Zhu, J. Pei, W. Duan, D. Liu and H. Li, *Nat. Commun.*, 2021, **12**, 6081.

8 H. Jo, J. Jang, H. J. Park, H. Lee, S. J. An, J. P. Hong, M. S. Jeong and H. Oh, *ACS Nano*, 2024, **18**, 30761–30773.

9 J. Li, W. Guo, Y. Qiao, L. Yao, Z. He, F. Wang, Y. Wang and F. Wang, *Appl. Phys. Lett.*, 2023, **123**, 151603.

10 G. Leonetti, M. Fretto, K. Bejtka, E. Sonia Olivetti, F. Candido Pirri, N. D. Leo, I. Valov and G. Milano, *Phys. Chem. Chem. Phys.*, 2023, **25**, 14766–14777.

11 G. S. How Thien, M. A. Mohd Sarjidan, N. Azrina Talik, B. Tong Goh, B. Kar Yap, Z. He and K.-Y. Chan, *Mater. Chem. Front.*, 2022, **6**, 3125–3142.

12 A. Krishnaprasad, D. Dev, S. S. Han, Y. Shen, H.-S. Chung, T.-S. Bae, C. Yoo, Y. Jung, M. Lanza and T. Roy, *ACS Nano*, 2022, **16**, 2866–2876.

13 J. V. Barth, H. Brune, G. Ertl and R. J. Behm, *Phys. Rev. B: Condens. Matter Mater. Phys.*, 1990, **42**, 9307–9318.

14 P. Li and F. Ding, *Sci. Adv.*, 2022, **8**, eabq2900.

15 N. A. Wasio, R. C. Quardokus, R. P. Forrest, C. S. Lent, S. A. Corcelli, J. A. Christie, K. W. Henderson and S. A. Kandel, *Nature*, 2014, **507**, 86–89.

16 P. Yang, S. Zhang, S. Pan, B. Tang, Y. Liang, X. Zhao, Z. Zhang, J. Shi, Y. Huan, Y. Shi, S. J. Pennycook, Z. Ren, G. Zhang, Q. Chen, X. Zou, Z. Liu and Y. Zhang, *ACS Nano*, 2020, **14**, 5036–5045.

17 S. Ghomi, A. Lamperti, M. Alia, C. S. Casari, C. Grazianetti, A. Molle and C. Martella, *Inorganics*, 2024, **12**, 33.

18 R. Ge, X. Wu, M. Kim, J. C. Lee and D. Akinwande, in *Emerging 2D Materials and Devices for the Internet of Things*, ed. L. Tao and D. Akinwande, Elsevier, 2020, pp. 1–28.

19 S. M. Hus, R. Ge, P.-A. Chen, L. Liang, G. E. Donnelly, W. Ko, F. Huang, M.-H. Chiang, A.-P. Li and D. Akinwande, *Nat. Nanotechnol.*, 2021, **16**, 58–62.

20 R. Ge, X. Wu, M. Kim, J. Shi, S. Sonde, L. Tao, Y. Zhang, J. C. Lee and D. Akinwande, *Nano Lett.*, 2018, **18**, 434–441.

21 B. Voigtländer, G. Meyer and N. M. Amer, *Surf. Sci. Lett.*, 1991, **255**, L529–L535.

22 D. D. Chambliss, *Phys. Rev. Lett.*, 1991, **66**, 1721–1724.

23 B. Voigtländer, *Phys. Rev. B: Condens. Matter Mater. Phys.*, 1991, **44**, 10354–10357.

24 E. Bianco, R. Rao, M. Snure, T. Back, N. R. Glavin, M. E. McConney, P. M. Ajayan and E. Ringe, *Nanoscale*, 2020, **12**, 12613–12622.

25 X. Zhang, J. Jiang, A. A. Suleiman, B. Jin, X. Hu, X. Zhou and T. Zhai, *Adv. Funct. Mater.*, 2019, **29**, 1906585.

26 M.-S. Kim, X.-H. Ma, K.-H. Cho, S.-Y. Jeon, K. Hur and Y.-M. Sung, *Adv. Mater.*, 2018, **30**, 1702701.

27 P. Cherin and P. Unger, *Acta Crystallogr.*, 1967, **23** 670–671.

28 W. Lin, P. Zhuang, D. Akinwande, X.-A. Zhang and W. Cai, *Appl. Phys. Lett.*, 2019, **115**, 073101.

29 R. Ge, X. Wu, L. Liang, S. M. Hus, Y. Gu, E. Okogbue, H. Chou, J. Shi, Y. Zhang, S. K. Banerjee, Y. Jung, J. C. Lee and D. Akinwande, *Adv. Mater.*, 2021, **33**, 2007792.

30 E. W. Lim and R. Ismail, *Electronics*, 2015, **4** 586–613.

31 J. Fatheema, T. Shahid, M. A. Mohammad, A. Islam, F. Malik, D. Akinwande and S. Rizwan, *RSC Adv.*, 2020, **10**, 19337–19345.

32 Y. Li, Z. Cui, Y. He, H. Tian, T. Yang, C. Shou and J. Liu, *Appl. Phys. Lett.*, 2022, **120**, 173104.

33 I. Horcas, R. Fernández, J. M. Gómez-Rodríguez, J. Colchero, J. Gómez-Herrero and A. M. Baro, *Rev. Sci. Instrum.*, 2007, **78**, 013705.